

Thermal and magnetic evolution of a crystallizing basal magma ocean in Earth's mantle

Nicolas A. Blanc^a, Dave R. Stegman^a, Leah B. Ziegler^a

^a*Institute for Geophysics and Planetary Physics, Scripps Institution of Oceanography,
University of California San Diego, La Jolla, California, USA*

Abstract

We present the thermochemical evolution of a downward crystallizing BMO overlying the liquid outer core and probe its capability to dissipate enough power to generate and sustain an early dynamo. A total of 61 out of 112 scenarios for a BMO with imposed, present-day Q_{BMO} values of 15, 18, and 21 TW and Q_r values of 4, 8, and 12 TW fully crystallized during the age of the Earth. Most of these models are energetically capable of inducing magnetic activity for the first 1.5 Gyrs, at least, with durations extending to 2.5 Gyrs; with final CMB temperatures of 4400 ± 500 K -well within current best estimates for inferred temperatures. None of the models with $Q_{BMO} = 12$ TW achieved a fully crystallized state, which may reflect a lower bound on the present-day heat flux across the CMB. BMO-powered dynamos exhibit strong dependence on the partition coefficient of iron into the liquid layer and its associated melting-point depression for a lower mantle composition at near-CMB conditions -parameters which are poorly constrained to date. Nonetheless, we show that a crystallizing BMO is a plausible mechanism to sustain an early magnetic field.

Email address: nblanc@ucsd.edu ()

Keywords: Basal magma ocean dynamo, Early Earth dynamo, Molten silicates

1 **1. Introduction**

2 A fundamental constraint on the thermal evolution of the Earth is that
3 of the presence of a magnetic field since at least 3.45 Ga (Tarduno et al.,
4 2010), and possibly even since 4.2 Ga (Tarduno et al., 2015). Some recent
5 estimates on the thermal conductivity of the Earth’s core imply estimates of
6 core heat flow on the order of 15 TW (de Koker et al., 2012; Pozzo et al.,
7 2012; Gomi et al., 2013) which favors a young (<500 Myr) inner core (Ol-
8 son, 2013; Davies, 2015; Labrosse, 2015; Nimmo, 2015). Since the buoyancy
9 sources associated with inner core nucleation (light element concentration
10 and latent heat) are the main sources of power dissipation for magnetic ac-
11 tivity generation for the current field (Buffett et al., 1996; Stevenson, 2003),
12 generating a geodynamo in the absence of an inner core (through secular
13 cooling of the core) poses significant challenges (Olson, 2013). Moreover,
14 thermal evolution models that incorporate high core heat flow, such as those
15 implied by higher thermal conductivity values, also imply extensive melting
16 of the mantle (i.e. a “thermal catastrophe”) (Korenaga, 2013, 2008; Driscoll
17 and Bercovici, 2014).

18 Sustaining a dynamo for >3 Gyrs in the absence of an inner core led
19 to the proposal of alternative mechanisms for powering a geodynamo, such
20 as the exsolution of light material across the core mantle boundary (CMB)
21 (ORourke and Stevenson, 2016; O’Rourke et al., 2017; Badro et al., 2016; Hi-
22 rose et al., 2017). Experimental determination of exsolution reactions (Badro

23 et al., 2016; Hirose et al., 2017; Badro et al., 2018) indicate this may be a vi-
24 able mechanism, however, there are still questions as to whether either would
25 provide sufficient power, duration, or be active during the period of interest
26 (Du et al., 2017, 2019; Badro et al., 2018).

27 Exsolution mechanisms explicitly occur across a metal-silicate interface
28 that is liquid on both sides (Badro et al., 2016, 2018), thus invoking a long-
29 lived basal magma ocean (BMO) atop the core (Labrosse et al., 2007; La-
30 neuville et al., 2018) which would initiate at mid-mantle depths and crys-
31 tallize downwards to the core. A giant impact as large as one suggested to
32 lead to the formation of the Moon may have been energetic enough that
33 Earth’s initial condition was completely molten (Canup and Asphaug, 2001;
34 Čuk and Stewart, 2012; Lock et al., 2018), however the initial depth of an
35 emergent BMO is subject to uncertainty in the equation of state of lower
36 mantle composition, its melting curve, the adiabatic gradient as determined
37 by its material properties, and the dynamics of phase separation (Stixrude
38 et al., 2009; De Koker and Stixrude, 2009; Boukaré et al., 2015; Boukaré and
39 Ricard, 2017; Wolf and Bower, 2018; Caracas et al., 2019). The scenario
40 of whether the BMO, if electrically conductive enough, could be capable of
41 generating a dynamo was explored as a potential mechanism for providing a
42 magnetic field during the early Earth (Ziegler and Stegman, 2013). Recent
43 theoretical calculations of the electrical conductivity of molten silicates at
44 P-T conditions appropriate for the CMB report values that support it as
45 a material that is sufficiently electrically conductive (Spaulding et al., 2012;
46 McWilliams et al., 2012; Soubiran and Militzer, 2018; Holmström et al., 2018;
47 Stackhouse et al., 2010; Scipioni et al., 2017).

48 The previous conceptual model for a BMO-powered dynamo (Ziegler and
49 Stegman, 2013) used an idealized phase diagram for the evolution of a crys-
50 tallizing basal magma ocean (Labrosse et al., 2007). In this study, we present
51 the thermochemical evolution of a downward crystallizing BMO (see Figure
52 1) using recent thermodynamic and mineral physics for molten silicates at
53 lower mantle P-T conditions (Stixrude, 2014; Boukaré et al., 2015; Caracas
54 et al., 2019), and their associated entropy budgets provide a more robust
55 measure of evaluating the circumstances under which the BMO played a role
56 in the magnetic evolution of early Earth. We constrain our models with the
57 early magnetic history of Earth and estimates of the current CMB tempera-
58 ture.

59 **2. Model and Methods**

60 We build upon an established theory for gross thermodynamics of the
61 Earth’s core with a solidifying inner core (Gubbins et al., 2003, 2004; Nimmo,
62 2015) and apply it to the scenario of a downward crystallizing BMO layer
63 overlying Earth’s core. We adapt an existing general 1D model for thermo-
64 chemical evolution of the Earth’s core (Davies, 2015) to study the evolution
65 and fractional crystallization of an FeO-enriched basal magma ocean (see Fig.
66 5C, D in (Caracas et al., 2019) for reference). We approximate the molten
67 layer to be a fluid in hydrostatic equilibrium with an adiabatic temperature
68 where a homogenously-mixed composition is maintained by vigorous convec-
69 tion everywhere outside thin boundary layers.

70 The global energy budget for the BMO-layer determines its evolution by
71 balancing the heat flux across the top of the layer (Q_{BMO}) against the sum

72 of all heat sources within the layer. While the energy budget contains infor-
73 mation about the cooling rate of the layer and, inevitably, the rate at which
74 it crystallizes, it lacks information about the dynamo as all magnetic energy
75 is converted into heat within the layer. Dynamo information is inherently
76 embedded in the entropy budget equations which relate all entropy sources
77 to the two most significant entropy sinks, thermal diffusion and Ohmic dis-
78 sipation; the power available to drive a dynamo is related to the latter.
79 Combining the energy budget with the associated entropy budget provides
80 sufficient information to describe and characterize the thermal and magnetic
81 evolution of the BMO over time.

82 *2.1. Energy Budget*

83 The total energy, Q_{BMO} , extracted through the top of the BMO layer by
84 the overlying solid mantle is the sum of all energy sources within the layer.
85 The complete energy budget can be written as

$$Q_{BMO} = Q_s + Q_g + Q_L + Q_r + Q_P + Q_H + Q_{CMB}, \quad (1)$$

86 which includes the secular cooling of the layer, Q_s , the gravitational poten-
87 tial energy released during solidification, Q_g , the latent heat generated as
88 the layer solidifies, Q_L , the heat due to radioactive decay, Q_r , the heat due
89 to a change in pressure due to thermal contraction, Q_P , and the heat of
90 reaction, Q_H . The contribution from Q_P, Q_H is negligible, they are only
91 included for completeness; and Q_{CMB} is heat attributed to the cooling of
92 the core. Following (Gubbins et al., 2003, 2004; Davies, 2015), the first four
93 terms except for Q_r can be related to the cooling rate, dT_r^{BMO}/dt , where
94 T_r^{BMO} is the temperature of the layer at the solidification front radius, r .

95 Indeed, these terms have been previously derived for the case of the solid-
 96 ifying inner core at length elsewhere (Gubbins et al., 2003, 2004; Nimmo,
 97 2015; Davies, 2015), thus we briefly summarize their analytical expressions
 98 below and, where necessary, explain the modification made in adapting these
 99 formulations to better represent the BMO scenario.

100 The first term in Eq. 1 describes the energy associated with the secular
 101 cooling of the layer and it can be expressed as

$$Q_s = - \int \rho C_p \frac{dT_r^{BMO}}{dt} dV, \quad (2)$$

102 where ρ and C_p are the density and specific heat capacity of the layer, re-
 103 spectively. This term is simply the amount of heat released as the layer cools
 104 volumetrically. The second term in 1 is related to the amount of gravitational
 105 energy released due to the re-distribution of lighter elements to the top of
 106 the layer, or equivalently the displacement of denser elements to the bottom
 107 of the layer, upon crystallization. It is given by

$$Q_g = \int \rho \psi \alpha_{BMO} \frac{Dc}{Dt} dV, \quad (3)$$

108 where ψ is the gravitational potential. The parameter α_{BMO} is a dimensional
 109 coefficient which specifies the sensitivity of the layer density to the enrich-
 110 ment of FeO, analogous to α_c described in (Gubbins et al., 2004) due to the
 111 presence of light elements in the core. It is given by

$$\alpha_{BMO} = -\frac{1}{\rho} \left(\frac{\partial \rho}{\partial c} \right)_{P,T} \approx \frac{\Delta \rho_{BMO}}{\rho_r^{BMO} \Delta c_{FeO}^l}, \quad (4)$$

112 where ρ_r^{BMO} is the density of the BMO layer at the solid-liquid interface
 113 radius r , and $\Delta \rho_{BMO}$ is the density jump across the interface due to the

114 change in concentration of the liquid, Δc_{FeO}^l , as it becomes progressively
 115 enriched in FeO upon solidification.

116 The change in concentration depends on the rate at which FeO is in-
 117 corporated into the solidifying bridgmanite phase which is controlled entirely
 118 by the partitioning coefficient, D_{FeO} . This allows for the following expres-
 119 sion, $\Delta c_{FeO}^l = c_{FeO}^l(1 - D_{FeO})$ which relates the amount of FeO in the liquid,
 120 c_{FeO}^l , to its partitioning coefficient. We estimate values for α_{BMO} (see Table
 121 2) using $\Delta\rho_{BMO} = 200 - 300 \text{ kg/m}^3$ from (Caracas et al., 2019) and two
 122 different partition coefficients for FeO: $D_{FeO} = 0.1$ (Nomura et al., 2011)
 123 and $D_{FeO} = 0.5$ (Andrault et al., 2012).

124 Lastly, the amount of gravitational energy released at the interface de-
 125 pends on the rate at which lighter elements are re-distributed to the top of
 126 the layer, Dc/Dt . Following (Gubbins et al., 2004), we relate this term to
 127 the rate at which the interface crystallizes,

$$\frac{Dc}{Dt} = Cc \frac{dr_{top}}{dt} = \frac{4\pi r_{top}^2 \rho_{top} \Delta c}{M_r^{BMO}}, \quad (5)$$

128 where r_{top} and ρ_{top} are the radius and the density at the top of the BMO
 129 layer, Δc is the change in concentration of the liquid layer, and M_r^{BMO} is the
 130 mass of the liquid layer.

131 The third term in 1 accounts for the latent heat generated and released
 132 at the interface as the layer solidifies and it depends on the rate at which
 133 this process occurs:

$$Q_L = 4\pi r_{top}^2 L_H \rho_{top} \frac{dr_{top}}{dt}, \quad (6)$$

134 where L_H is the latent heat of reaction which is assumed to be constant. The
 135 last term in 1 is simply the heat generated within the volume of the BMO

136 layer by the decay of radioactive elements. Considering a density ρ and a
 137 volumetric heating rate, h , over a volume, V , this term can be written as

$$Q_r = \int \rho h dV. \quad (7)$$

The heat production is time-dependent according to the assumed BSE concentrations, long-lived radioactive decay energies and halflives, which are given in Table 1. Making use of the formulations presented above, the total energy budget 1 for a crystallizing BMO layer can be expressed as follows

$$\begin{aligned} Q_{BMO} &= - \int \rho C_p \frac{dT_r^{BMO}}{dt} dV + \int \rho \psi \alpha_{BMO} \frac{Dc}{Dt} dV \\ &+ 4\pi r_{top}^2 L_H \rho_{top} \frac{dr_{top}}{dt} + \int \rho h dV + M_{core} C_{p(core)} \frac{dT_r^{BMO}}{dt} \\ &= Q_s + Q_g + Q_L + Q_r + Q_{CMB} \end{aligned} \quad (8)$$

138 2.2. BMO solidification model

139 In this work, we consider a BMO layer overlying the liquid core crystalliz-
 140 ing from the top down towards the CMB, whose thickness is determined by
 141 the intersection of the adiabat and the melting curve as shown schematically
 142 in Figure 1. As the layer cools, the adiabat intersects the melting curve at
 143 greater depths causing the layer to shrink. The initial thickness of the layer
 144 is determined by the initial temperature; here, we define two different values
 145 for the initial temperature of the layer resulting in two initial thicknesses:
 146 $r_0^{top} = 4242$ km and $r_0^{top} = 4458$ km.

147 We implement a lower mantle adiabat with two different gradients, and
 148 utilize the melting curve for a peridotite mantle composition (Fiquet et al.,
 149 2010; Stixrude, 2014). Two different melting point depressions at the CMB,
 150 $T_m^0 = 700$ K and $T_m^0 = 1100$ K are imposed onto the undepressed melting

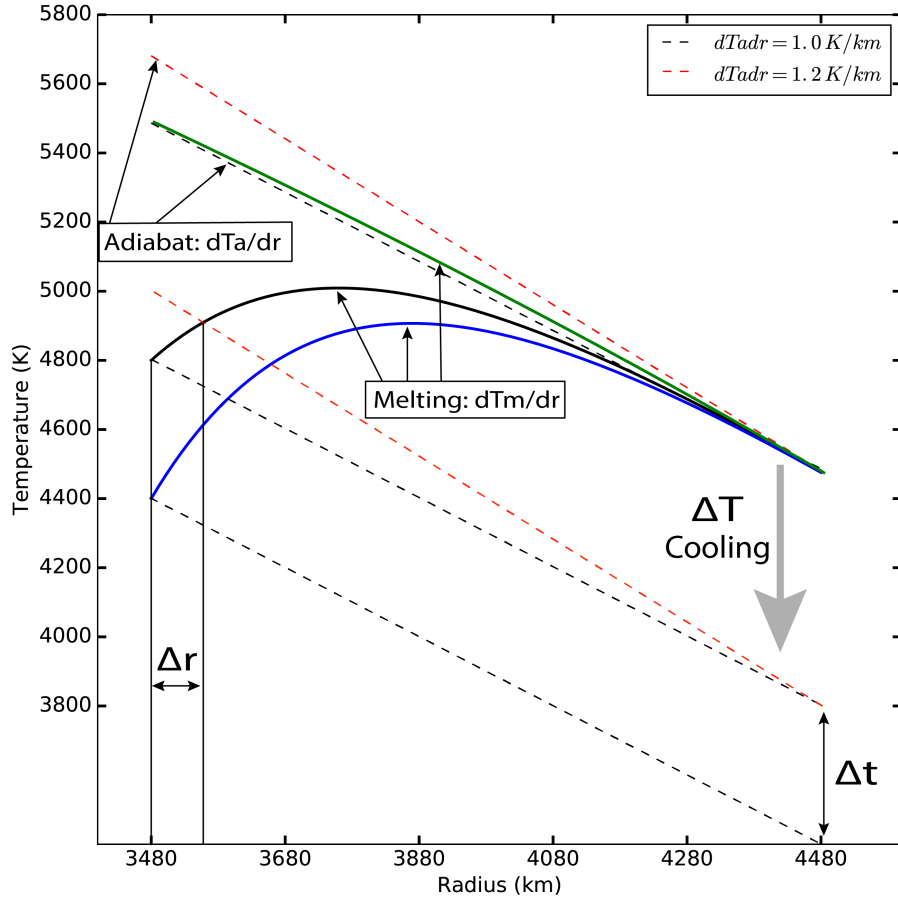


Figure 1: BMO thermal evolution diagram. The thickness of the BMO layer is defined by the intersection of the adiabat, T_a , and the melting curve, T_m . The corresponding temperature at the CMB is determined by tracking the adiabat to the appropriate radius. Secular cooling of the layer over time moves the adiabat to lower temperatures, intersecting the melting curve at greater depths thus crystallizing the layer downward toward the CMB. Imposing a larger melting point depression at the CMB to the melting curve (black versus blue solid curves) prolongs the life of the BMO layer as it is required to cool an additional amount of time, Δt , to fully crystallize. Moreover, at a time, t , two different adiabats (red and black dashed lines) will intersect a given melting curve at different points changing the thickness of the BMO layer at that point in time by an amount Δr .

Table 1: Input parameters.

Definition	Symbol	Units	Value	Reference
Density	ρ	Kg m ⁻³		(Dziewonski and Anderson, 1981)
Density jump	$\Delta\rho_{BMO}$	Kg m ⁻³	200 - 300	(Caracas et al., 2019)
CMB pressure		GPa	135	
Mantle specific heat	$C_{p_{mantle}}$	J Kg ⁻¹ K ⁻¹	1000	(Labrosse et al., 2007)
Core specific heat	$C_{p_{core}}$	J Kg ⁻¹ K ⁻¹	860	(Labrosse et al., 2007)
Mass of Core	M_{core}	Kg	2×10^{24}	(Labrosse et al., 2007)
Adiabatic gradient	dT_a/dr	K / km	1.0/1.2	
Entropy of melting per unit mass	Δs	J Kg ⁻¹ K ⁻¹	300	(Labrosse et al., 2007)
Melting temperature at the CMB		K	5400	(Fiquet et al., 2010)
Melting-point depression at the CMB	T_m^0	K	700 / 1000	
Thermal conductivity of the mantle	k	W m ⁻¹ K ⁻¹	8	(Labrosse et al., 2007)
Initial FeO concentration		wt%	15.99	(Caracas et al., 2019)
FeO partition coefficient	D_{FeO}		0.1 / 0.5	(Nomura et al., 2011; Andraut et al., 2012)

151 curve (green curve in Figure 1) to represent the depression induced by the
152 progressive enrichment of the liquid layer in FeO as it crystallizes. The
153 density of the layer is estimated to be similar to that of the current lower
154 mantle for which we utilize a polynomial fit to the Preliminary reference
155 Earth model (PREM) (Dziewonski and Anderson, 1981).

156 We take the initial concentration of FeO in the liquid to be that of (Caracas
157 et al., 2019) for a pyrolitic melt after 50% crystallization of bridgmanite
158 and allow it to evolve using two different (end-member) values for the parti-
159 tion coefficient: $D_{FeO} = 0.5$ (Andraut et al., 2012), and $D_{FeO} = 0.1$ (Nomura
160 et al., 2011). However, since the behavior of D_{FeO} has only been character-
161 ized for Fe partitioning between bridgmanite and liquid compositions which
162 have relatively modest Fe concentrations, we would expect D_{FeO} to deviate
163 from these measured values once the system has evolved to be heavily Fe
164 enriched. Accordingly, we adopt a conservative threshold at $c_{FeO}^l = 50 \text{ wt}\%$
165 for the interpretation of our model results once the concentration of FeO in

166 the liquid exceeds 50 *wt%*, as we anticipate the partition coefficient for such a
167 state to deviate from the constant value being applied. All input parameters
168 are presented in Table 1.

169 The evolution of all models is largely controlled by the amount of heat
170 being extracted by the solid mantle from the top of the BMO layer and the
171 amount of radiogenic heat produced within the layer. Henceforth we refer to
172 the combination of these two parameters as “cooling history”. The internal
173 heating of the mantle corresponds to a Bulk Silicate Earth (BSE) model
174 (McDonough and Sun, 1995) comprises of the decay energies for the 4 long
175 lived radioactive isotopes (U235, U238, Th232, and K40) in the appropriate
176 ratios. The radiogenic heat production over time is prescribed by the sum of
177 the abundance and decay energies for the 4 isotopes and their corresponding
178 half-lives, based upon the present day heat production for the BSE of 20 TW.
179 Approximately 8 TW of the total BSE complement is assumed to reside in
180 the continental crust, and the remaining 12 TW (out of the 20 TW total)
181 therefore resides within the mantle, for which we consider 3 scenarios (4, 8
182 or 12 TW) for how much is contained within the BMO, representing 33%,
183 67%, or 100% of the available heat production shown as dashed curves in
184 Figure 2. The complement of radiogenic heat producing elements initially in
185 the BMO are assumed to remain in the BMO for its entire evolution, and
186 thus for models that have completely solidified, the entirety of the radiogenic
187 heating would be contained within a very thin layer in the mantle atop the
188 CMB.

189 The cooling of the BMO, $Q_{BMO}(t)$, is controlled by a cooling history that
190 is prescribed at the interface between solid and liquid mantle with a present-

Table 2: Model results from all the different Q_{BMO}/Q_r setups probed in this study. The input parameters for each run (1-16) within a given setup are the adiabatic gradient (dTa/dr) in K/km, the partition coefficient for FeO (D_{FeO}), compositional coefficient (α_{BMO}), and the imposed depression on the melting curve (T_m^0). Given our conservative cutoff, we report the available entropy due to Ohmic dissipation (E_Φ) at $c_{FeO}^l = 50 wt\%$ in MW/K, and the time when this cutoff is reached (t_X), along with the time when E_Φ falls below zero. The time it takes each model to fully crystallize (if successful) is given by t_{BMO} and the final temperature at the CMB for each case is given by T_{CMB}^{final} .

COMBO #	1	2	3	4	5	6	7	8	9	10	11	12	13	14	15	16
dTa/dr	1	1	1	1	1	1	1	1	1.2	1.2	1.2	1.2	1.2	1.2	1.2	1.2
D_{FeO}	0.1	0.1	0.1	0.1	0.5	0.5	0.5	0.5	0.1	0.1	0.1	0.1	0.5	0.5	0.5	0.5
α_{BMO}	0.3	0.3	0.4	0.4	0.4	0.4	0.3	0.3	0.3	0.3	0.4	0.4	0.4	0.4	0.3	0.3
T_m^0	700	1100	700	1100	700	1100	700	1100	700	1100	700	1100	700	1100	700	1100
Cooling history model: ★ $Q_{BMO}^{present} = 15$ TW, $Q_r = 4$ TW, $Q_{CMB}^{present} = 11$ TW																
E_Φ	280	215	351	21	1	-30	-9	-35	265	182	324	222	-40	-80	-50	-83
t_X (Myr)	1050	1390	1070	1430	1690	2550	1670	2520	1540	1860	1600	1920	2600	3590	2560	3540
t_Φ (Myr)	2200	2810	2370	3080	1690	2210*	1620*	2120*	2920	3160	3240	3470	2250*	2560*	2140*	2450*
t_{BMO} (Myr)	2420	4070	2480	4180	2330	3930	2310	3890	4020		4180		3820		3750	
T_{CMB}^{final} (K)	4258	4310	4279	4334	4228	4279	4220	4270	4500	4433	4533	4458	4453	4401	4438	4390
Cooling history model: ■ $Q_{BMO}^{present} = 18$ TW, $Q_r = 4$ TW, $Q_{CMB}^{present} = 14$ TW																
E_Φ	453	360	566	434	49	15	34	6	484	364	584	435	18	-24	7	-32
t_X (Myr)	750	960	760	980	1160	1620	1150	1610	1060	1250	1100	1280	1690	2170	1660	2150
t_Φ (Myr)	1560	2100	1610	2250	1300	1700	1250	1640	2200	2500	2390	2700	1760	2050*	1690	1980*
t_{BMO} (Myr)	1590	2370	1630	2420	1540	2310	1530	2290	2430	3350	2510	3440	2330	3230	2300	3190
T_{CMB}^{final} (K)	3668	3684	3690	3705	3638	3654	3630	3645	3908	3864	3943	3894	3862	3823	3848	3811
Cooling history model: ◆ $Q_{BMO}^{present} = 18$ TW, $Q_r = 8$ TW, $Q_{CMB}^{present} = 10$ TW																
E_Φ	284	217	347	263	1	-31	-7	-35	267	183	322	220	-43	-81	-48	-84
t_X (Myr)	1090	1460	1120	1490	1770	2730	1750	2700	1610	1960	1670	2020	2780	3920	2730	3850
t_Φ (Myr)	2290	2940	2470	3220	1780	2360*	1710*	2270*	3050	3330	3370	3640	2400*	2740*	2290*	2630*
t_{BMO} (Myr)	2570	4490	2640		2480	4320	2450	4270	4410				4170		4100	
T_{CMB}^{final} (K)	4342	4399	4363	4418	4312	4366	4303	4357	4583	4502	4613	4525	4536	4471	4522	4460
Cooling history model: ● $Q_{BMO}^{present} = 21$ TW, $Q_r = 8$ TW, $Q_{CMB}^{present} = 13$ TW																
E_Φ	488	390	592	464	60	25	45	15	517	398	623	470	30	-14	19	-22
t_X (Myr)	740	950	760	970	1150	1610	1140	1600	1060	1240	1090	1270	1680	2160	1650	2140
t_Φ (Myr)	1550	2100	1600	2240	1310	1720	1270	1670	2220	2530	2390	2730	1780	2090*	1720	2030*
t_{BMO} (Myr)	1580	2360	1620	2410	1540	2300	1520	2280	2420	3340	2500	3430	2320	3220	2290	3180
T_{CMB}^{final} (K)	3671	3686	3693	3707	3642	3657	3633	3648	3911	3866	3946	3896	3865	3825	3851	3812
Cooling history model: ▲ $Q_{BMO}^{present} = 21$ TW, $Q_r = 12$ TW, $Q_{CMB}^{present} = 9$ TW																
E_Φ	303	234	365	275	5	-28	-2	-32	280	196	332	230	-39	-79	-45	-81
t_X (Myr)	1100	1480	1130	1520	1810	2820	1790	2790	1650	2010	1710	2070	2870	4090	2820	4020
t_Φ (Myr)	2340	3040	2530	3310	1850	2480*	1780*	2400*	3150	3470	3470	3780	2510*	2900*	2410*	2800*
t_{BMO} (Myr)	2640		2720		2550		2520	4480					4360		4290	
T_{CMB}^{final} (K)	4379	4432	4401	4452	4350	4404	4342	4396	4617	4533	4644	4556	4575	4503	4561	4492

* represents the last instance in time when $E_\Phi > 0$.

191 day value of 15, 18, and 21 TW shown as solid curves in Figure 2. Thus,
 192 the core heat flow across the CMB, Q_{cmb} , at the present day spans values
 193 between 9-14 TW, which is the difference between Q_{BMO} and Q_r for the
 194 cooling histories considered in Table 1. The differences between Q_{BMO} and
 195 Q_r for the various combinations also imply higher or lower secular cooling
 196 rates for the mantle, as the larger value chosen for Q_r leaves a smaller amount
 197 of the available 12 TW for heating the mantle above the BMO. For example,
 198 Q_r of 8 TW in the BMO leaves only 4 TW in the solid mantle, leading
 199 to faster secular cooling of the mantle which would presumably drive faster
 200 secular cooling of the core, and hence this value of Q_r is used in combination
 201 with larger Q_{BMO} values of 18 TW and 21 TW, corresponding to Q_{cmb} values
 202 of 10 and 13 TW, respectively.

203 *2.3. Entropy budget*

204 As mentioned above, the energy budget alone provides enough informa-
 205 tion to determine the thermal evolution of the BMO layer. However, in
 206 order to fully characterize its magnetic evolution and, ultimately, determine
 207 the feasibility of dynamo activity, the entropy balance equations are required.
 208 Most importantly, the entropy associated with thermal conduction down an
 209 adiabat, E_{κ} , and the Ohmic heating play crucial roles in determining if a
 210 dynamo is energetically favorable once all sources of entropy are considered.
 211 An equation analogous to 1 can be written for the entropy budget identifying
 212 both sources and sinks, and cases for the core have been extensively derived
 213 elsewhere (Gubbins et al., 2003, 2004; Nimmo, 2015). Below, we only present
 214 their final formulations and describe any changes made in adapting them to

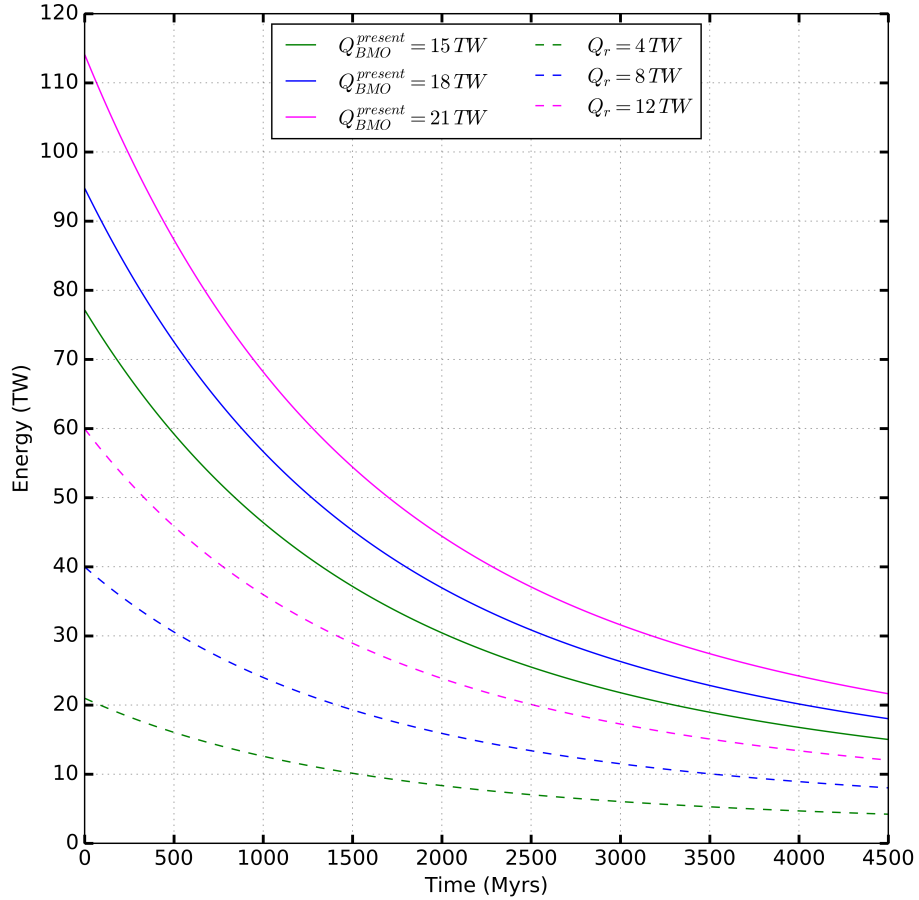


Figure 2: Cooling histories. The three different cooling histories imposed for all model runs (#1-16 in Table 2) representing 15, 18, and 21 TW present-day, adiabatic heat flux across the top of the BMO layer are shown as solid lines. Dashed lines show the three different radiogenic heating curves 4, 8, and 12 TW resulting from assuming that roughly 30%, 70%, and 100% of the BSE radioactive element budget are initially sequestered within the BMO layer.

215 describe our model. The entropy budget is as follows

$$E_s + E_g + E_r + E_L + E_P + E_H = E_k + E_\Phi, \quad (9)$$

216 where E_s , E_g , E_r , E_L , E_P , and E_H are the sources and E_k , E_Φ are the sinks;
 217 k is the thermal conductivity of the layer, and Φ represents the combined
 218 viscous and Ohmic dissipation, though the former is assumed to be negligible
 219 (Nimmo, 2015). The small contributions from E_P and E_H are also ignored in
 220 this work. Excluding these terms, the analytical expression for the entropy
 221 budget is as the following

$$\begin{aligned} & - \int \rho C_p \left(\frac{1}{T_c} - \frac{1}{T} \right) \frac{dT_r^{BMO}}{dt} dV + \frac{Q_g}{T} + \int \rho h \left(\frac{1}{T_c} - \frac{1}{T} \right) dV \\ & - \frac{4\pi r_i^2 L_H (T_i - T_c)}{(dT_m/dP - dT/dP) T_c^2 g} \frac{dT_r^{BMO}}{dt} = \int k \left(\frac{\nabla T}{T} \right)^2 dV + \int \frac{\Phi}{T} dV, \end{aligned}$$

222 which is comparable to 8 except for the Carnot efficiency term, $(1/T_c - 1/T)$.

223 The criteria of $E_\Phi > 0$ is commonly used for determining whether the
 224 model can generate a dynamo subject to the same assumptions that govern
 225 the applicability of this approach to core dynamics (Gubbins et al., 2004;
 226 Nimmo, 2015; Buffett et al., 1996; Labrosse, 2003), that the fluid is elec-
 227 trically conductive, rapidly rotating, and undergoing vigorous convection to
 228 remain adiabatic and homogenous, all of which are also appropriate for the
 229 scenario of a basal magma ocean. This framework is easily adaptable to
 230 determining the Ohmic dissipation within a BMO layer. The expression for
 231 the first three terms remain the same but the integration bounds must be
 232 adapted to encompass the evolving thickness of the BMO layer. However,
 233 the term for entropy production due to the release of latent heat at the in-
 234 terface, E_L , which depends on the cooling rate of the layer and the difference

235 between the slopes of the adiabat and the melting curve, is different to the
236 analogous core case.

237 For the case of the inner core growing outward, the adiabat and the melt-
238 ing curve are anchored at two distinct temperatures; the CMB temperature
239 for the adiabat and the interface (inner-core boundary (ICB)) temperature
240 for the liquidus. However, for the BMO layer crystallizing downward to-
241 wards the CMB, both the adiabat and melting curve are anchored at the
242 same point. This results in $(T_i - T_c)$ in E_L to be zero. Another way to
243 think about this is to consider where the latent heat is being generated. In
244 the case of the core, latent heat is released at the ICB which drives convec-
245 tive motions throughout the liquid outer core directly above; but for a BMO
246 layer, the latent heat is generated at the top of the liquid layer, so it does
247 not contribute to convection in the liquid below. Finally, it is clear from
248 these equations that aside from requiring entropy sources to be sufficiently
249 energetic to power the dynamo, E_k cannot be too large (i.e. large values of
250 k) as this would result in most of the entropy being conducted away along
251 the adiabat and not be available to power a dynamo.

252 **3. Results**

253 A total of 112 models were simulated, but only 61 models fully crystal-
254 lized their BMO layer during the age of the Earth. The input parameters
255 for all model runs and their diagnostic outputs are provided (see Table 1
256 and 2, respectively). The final CMB temperature for all models that fully
257 crystallized during the age of the Earth falls within the plausible range for
258 present-day best-estimate for inferred temperatures at the CMB (Anzellini

259 et al., 2013) as shown in Figure 3.

260 The longevity of the BMO layer varies greatly between models, ranging
261 from short-lived layers crystallizing in 1.5 Gyrs to long-lived layers taking as
262 much as 4.5 Gyrs to fully crystallize. The dominant parameters controlling
263 the thermal evolution of the BMO layer are the imposed depression on the
264 melting curve and the adiabatic gradient; these effects are shown schemat-
265 ically by arrows in Figure 3. For a given cooling history, imposing a larger
266 melting-point depression extends the life of the BMO layer but it has a neg-
267 ligible effect on the final CMB temperature. However, introducing a steeper
268 adiabatic gradient ($dTa/dr = 1$ K/km for filled marker vs $dTa/dr = 1.2$
269 K/km for unfilled markers in Figure 3) not only extends the time it takes
270 the BMO layer to fully crystallize, but it also results in a hotter present-day
271 CMB temperature. Changing both parameters simultaneously appears to
272 have an almost linear additive effect.

273 The general trend observed in Figure 3 is primarily controlled by the
274 total heat budget available to drive the BMO evolution, as defined by the
275 particular cooling history imposed (i.e. combination of $Q_{BMO}^{present}$ and Q_r from
276 Figure 2). Indeed, the fastest cooling models, those on the bottom left,
277 have a bigger heat budget than the slower cooling models on the top right.
278 Moreover, our choice of curves for Q_{BMO} and Q_r and their inherent curvatures
279 causes the effects due to melting-point depression and adiabatic gradient to
280 be more pronounced on the slower cooling models, with some of these taking
281 as much as 4.5 Gyrs to fully crystallize. A batch of 32 models with Q_{BMO}
282 = 12 TW and $Q_r = 4$ and 8 TW (corresponding to $Q_{CMB} = 8$ and 4 TW,
283 respectively) were probed and none successfully crystallized the entirety of

284 their BMO layer during the 4.5 Gyrs time window. Indeed, 19 other models
285 with the cooling histories reported here were also unsuccessful (see Table 2).

286 Given the large group of successful models, we focus on two models which
287 best represent the extensive range of evolution scenarios generated by our
288 choices of parameters. Moreover, these reference models resemble the model
289 proposed by (Ziegler and Stegman, 2013). The complete temperature, energy,
290 and entropy evolution for models #1 and #15 are respectively shown in the
291 top, middle, and bottom panels of Figure 4.

292 The evolution of the temperature and the interface radius between the
293 liquid, crystallizing BMO layer and the solid mantle above for each model
294 is shown in Figure 4A and B. Both models share the same imposed cooling
295 history with $Q_{BMO} = 15$ TW and $Q_r = 4$ TW, but have two different dTa/dr
296 values. The initial thickness of the BMO (i.e. interface radius) is defined by
297 the intersection of the melting curve (solid black line) with the adiabat (see
298 Figure 1), and its evolution is controlled by the cooling rate of the layer
299 which is directly dominated by the amount of heat being extracted from the
300 layer, as prescribed by the cooling history curve. As the layer cools over
301 time, the adiabat evolves to lower temperatures (shown as colored dashed
302 lines) intersecting the melting curve at greater depths causing the interface
303 radius to decrease and the liquid layer to shrink towards the CMB. Indeed,
304 the retarding effect dTa/dr has on the evolution of the layer (shown in Figure
305 3) is evident here as model #1 crystallizes about 1 Gyr sooner than model
306 #15 with the steeper adiabatic gradient.

307 All the terms in the energy budget outlined in Eq. 8 for both models
308 including an imposed core cooling (yellow curve) term are shown in Figure

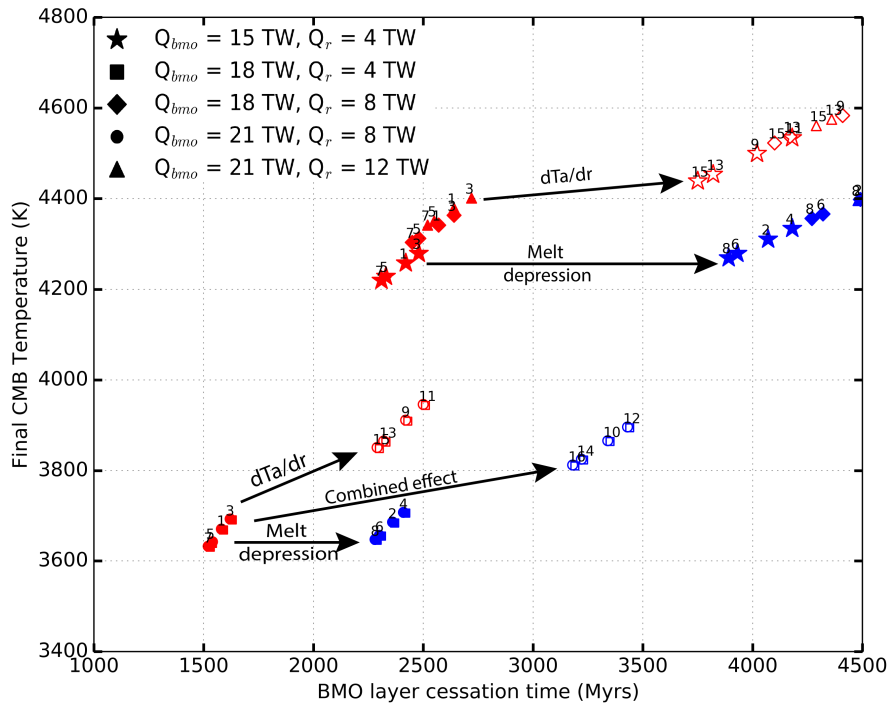


Figure 3: Final CMB temperature. The present-day CMB temperature for all models that successfully crystallized during the age of the Earth are plotted at their corresponding crystallization time. Both adiabatic gradients, $dTa/dr = 1$ (filled markers) and $dTa/dr = 1.2$ (unfilled markers) and both melting point depressions to the melting curve, 700 K (red) and 1100 K (blue) are shown. Schematic arrows show the effect of either parameter in the longevity of the BMO layer for any model run (depicted by the model run numbers) within a given model setup (markers in legend).

309 4C and D. The most energetic source during the evolution of the BMO layer
310 is the latent heat released as the layer crystallizes, while gravitational rear-
311 rangement and secular cooling terms are small. The amount of latent heat
312 released is the largest during the first billion years of evolution as this is when
313 the crystallization rate is the fastest before being retarded by the imposed
314 melting-point depression on the melting curve. When the layer crystallizes
315 to a thickness of $\approx 200 - 300$ km, the latent heat term becomes comparable
316 to the radiogenic heating and the crystallization rate decreases significantly.
317 Once the layer reaches the CMB, the radiogenic elements are assumed to
318 be trapped in a thin layer atop the CMB, while Q_L and Q_g terms become
319 zero which results in a corresponding jump in core heat flow. The remaining
320 thermal evolution is primarily accommodated by secular cooling of the core
321 according to the prescribed thermal history model (Q_{BMO}) and the assumed
322 heat capacity of the core, resulting in the final T_{CMB} values shown in Figure
323 3.

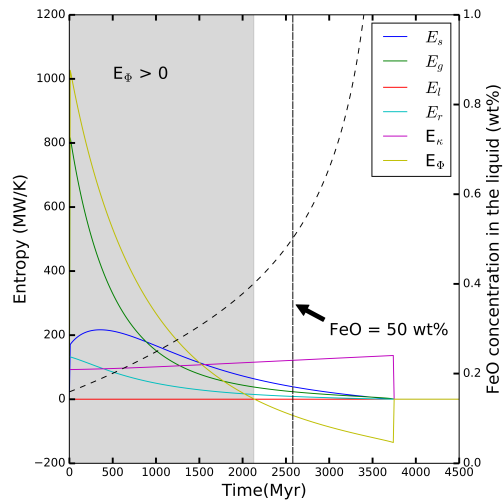
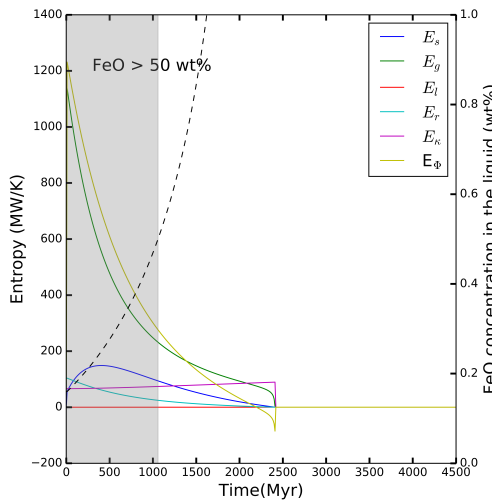
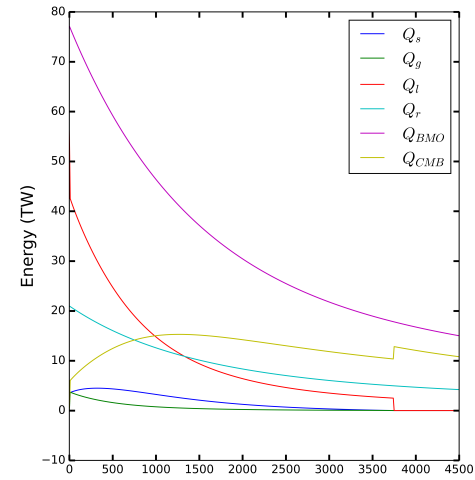
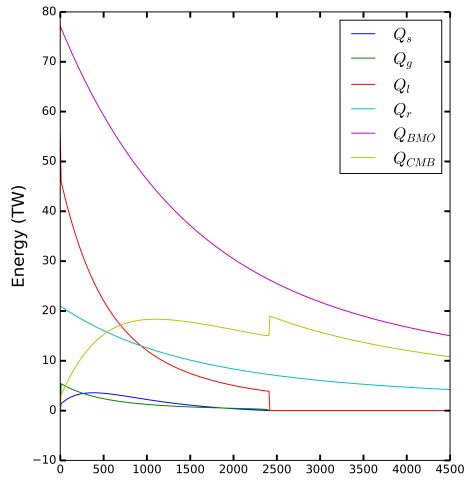
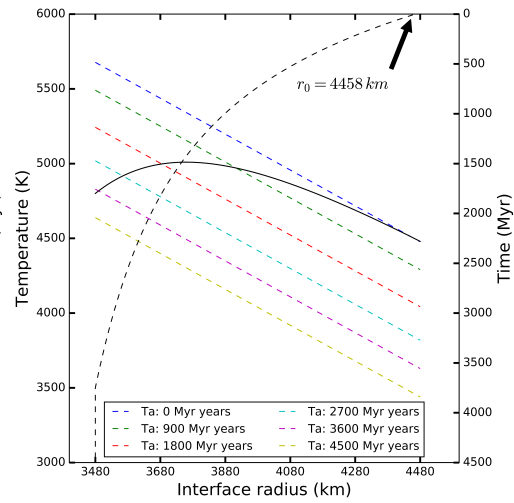
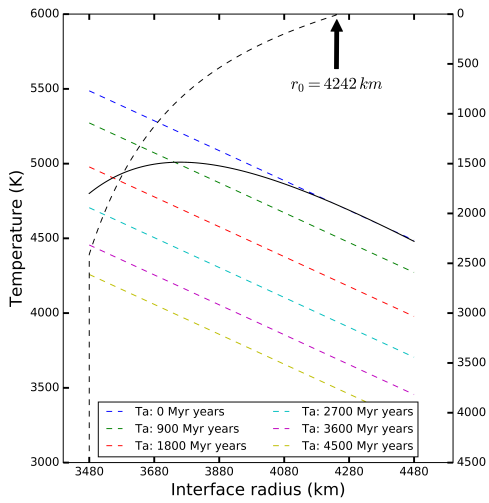


Figure 4: BMO layer evolution. Representative models with $Q_{BMO} = 15$ TW and $Q_r = 4$ TW showing the temperature, energy, and entropy evolution of a 762-km and 978-km thick BMO layer for Models #1 (left column) and Model #15 (right column), respectively. The evolution of the temperature and thickness of the BMO layer over time controlled by the different adiabatic gradients ($dTa/dr = 1$ K/km for Model #1 and $dTa/dr = 1.2$ K/km for Model #15) are shown on panel A and B, respectively. Each term in the energy budget outlined in Eq. 1 is plotted in C and D for both models over time. The evolution of the associated entropy terms (solid curves) and evolution of the FeO concentration (dashed curve) over time are shown in E and F. Shaded regions show the time interval where $E_\Phi > 0$ while the FeO concentration in the liquid is below 50 wt% (panel E), and last instance when $E_\Phi > 0$ in panel F (i.e. when FeO concentration in run #15 reaches 50%, $E_\Phi < 0$).

The terms in the entropy budget outlined in Eq. 9 for each model are shown in Figure 4E and F, along with the corresponding evolution of the FeO concentration in the liquid layer. As described in the Methods section, the latent heat term is zero for the scenario being considered here. While the gravitational term is small in the energy budget, it is the main contributor of entropy to the system (green curve), with the secular (blue curve) and radiogenic (light blue curve) terms contributing marginally. The cumulative total of these entropy sources is balanced against both thermal conduction (magenta curve) and Ohmic dissipation (yellow curve), which are the entropy sinks in the system.

The entropy of thermal conduction is approximately constant and scales with the choice of thermal conductivity, which is 8 W/m/K for these models. Both models sustain $E_\Phi > 0$ for the first ≈ 2 billions years, indicating a dynamo would be present in both models over that period of time. However, for BMO dynamos, we consider an additional criteria of whether D_{FeO} is still consistent with the system once it has become highly enriched in Fe. Consequently, we adopt a value of $c_{FeO}^l = 50$ wt% for this threshold, which

342 is shown in the shaded regions. Model #15 (Figure 4F) falls below $E_\Phi = 0$
 343 before this threshold is reached, and for such models as this, we report their
 344 dynamo cessation time (starting from $t_\Phi=0$) as the last instance when $E_\Phi >$
 345 0. In contrast, Model #1 (Figure 4E) reaches the threshold while E_Φ is still
 346 positive, and for models that encounter this situation, we report the time
 347 they reach this threshold as their dynamo cessation.

348 We consider this threshold value as a conservative estimate given that
 349 E_Φ is well above zero when this point is reached and it would be likely for
 350 a dynamo to be operating beyond this time. The partitioning of Fe into the
 351 remaining liquid at the solidification front is the mechanism for generating
 352 gravitational entropy, which is the dominant term in the entropy budget and
 353 controls the magnitude of the Ohmic dissipation. The rate at which the
 354 fluid is enriched with Fe, and speed at which the threshold value is reached,
 355 is determined by the value of D_{FeO} . Model #1, with $D_{FeO} = 0.1$, results
 356 in c_{FeO}^l increasing more rapidly (dashed line in Figure 4E) than measured
 357 increases of c_{FeO}^l in Model #15, with $D_{FeO} = 0.5$ (dashed line in Figure 4F).
 358 Therefore, the dynamo generated by model #1 (Figure 4E) is roughly 20%
 359 more energetic than that of model #15 (Figure 4F).

360 The amount of entropy available to sustain a dynamo varies among all
 361 successful models. Model results for all runs including the available entropy
 362 (at $c_{FeO}^l = 50 wt\%$), their corresponding dynamo and BMO cessation times,
 363 and their final CMB temperatures are shown in Table 2. Figure 5 shows the
 364 amount of Ohmic dissipation at the time the BMO composition encountered
 365 the threshold value of $c_{FeO}^l = 50 wt\%$ for all models that fully crystallized
 366 within the age of the Earth. The two clear populations of models shown

367 in Figure 5 are primarily controlled by the two, end-member values for the
 368 partition coefficient of FeO. Models with $D_{FeO} = 0.1$ (Nomura et al., 2011)
 369 give rise to long-lived dynamos with lower Ohmic dissipation while those
 370 with $D_{FeO} = 0.5$ (Andrault et al., 2012) result in dynamos that are short-
 371 lived and larger values of E_{Φ} . Both scenarios, however, result in models with
 372 sufficiently large E_{Φ} values for the first 1.5 Gyrs -implying an active dynamo
 373 during this time.

374 Combining our results from Figure 3 for how long it takes the BMO layer
 375 to fully crystallize and, in each of those models, how long a dynamo would
 376 be active from Figure 5, we can see there exists a wide range of scenarios for
 377 a BMO dynamo as shown in Figure 6. These scenarios can be summarized
 378 in four distinct populations: Short-lived BMO with (1) short-lived, intense
 379 dynamo, and (2) long-lived, weaker dynamo; and long-lived BMO with (3)
 380 short-lived, intense dynamo, and (4) long-lived, weaker dynamo.

381 The intensity of the dynamo is regulated by the value of D_{FeO} while
 382 the time required for the layer to completely solidify is controlled by both
 383 melting-point depression and the choice of adiabatic gradient. Those models
 384 with the smaller melting-point depression (e.g. $T_m^0 = 700$ K) and a partition
 385 coefficient $D_{FeO} = 0.1$ result in short-lived BMO layers with roughly 60%
 386 more entropy available (at $c_{FeO}^l = 50$ wt%) to sustain a dynamo compared
 387 to the cases with $D_{FeO} = 0.5$. A smaller D_{FeO} value results in faster Fe
 388 enrichment of the liquid layer and correspondingly higher values of entropy
 389 generated due to the larger density jump at the interface (e.g. larger E_g
 390 term). Indeed, extending the timescale for solidification of the BMO, by
 391 imposing a larger melting-point depression, increases the amount of entropy

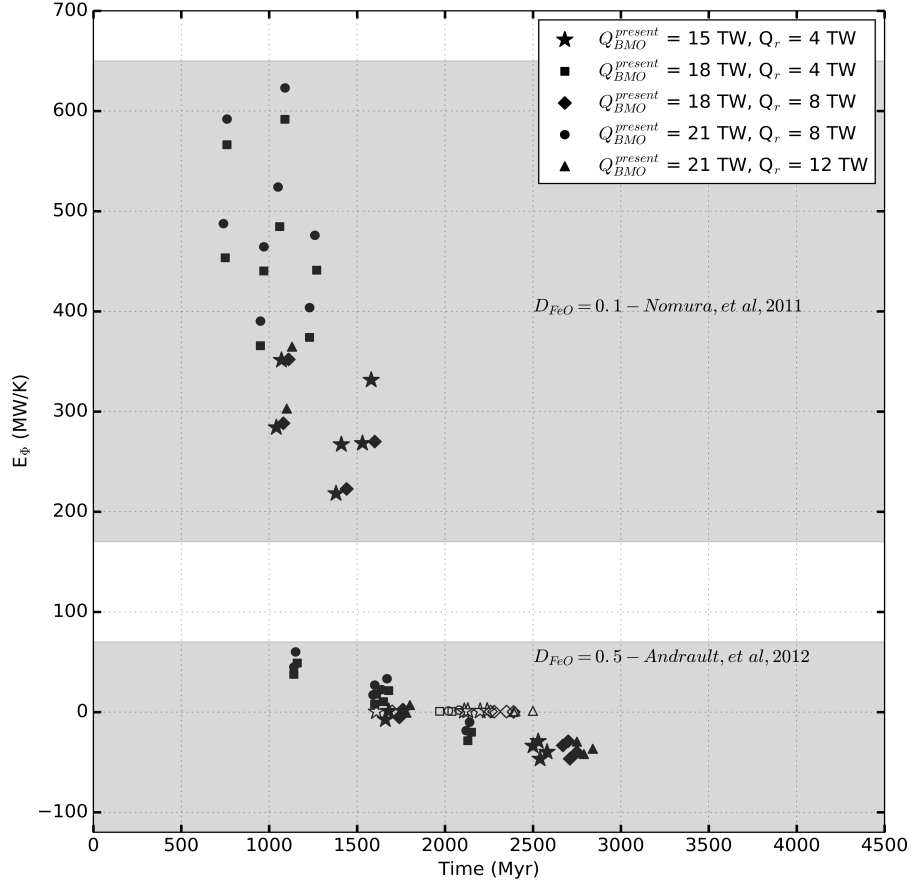


Figure 5: Entropy of Ohmic dissipation over time for all models (at $c_{FeO}^l = 50 \text{ wt}\%$) whose BMO layer fully crystallized during the age of the Earth plotted in black (filled). For models with $E_\Phi < 0$ at this cutoff, their entropy value is plotted at the last time when it was positive in black (unfilled). Markers indicate the five difference $Q_{BMO} - Q_r$ scenarios imposed as described in the text. Two distinct clusters, indicated by the shaded regions, capture the influence of the two different partition coefficient values.

392 available to sustain magnetic activity for a longer period of time. It is plau-
393 sible to have models extending the entire shaded area in Figure 6 through a
394 different combination of allowable model parameters and a less conservative
395 cutoff (i.e. $> c_{FeO}^l = 50 wt\%$).

396 4. Discussion

397 The present-day CMB temperature for all successful models shown here
398 (Figure 3) falls within a plausible value (4000 ± 500 K) for the best estimates
399 up to date (Anzellini et al., 2013). The thermal evolution of a BMO layer
400 atop the liquid core over time is heavily dominated by two parameters: the
401 adiabatic gradient in the liquid, and the melting curve for a lower mantle
402 composition; most importantly how depressed this curve becomes at near-
403 CMB pressures and temperatures.

404 The entropy budget of a BMO-powered dynamo are heavily dominated
405 by the choice in partition coefficient for FeO in the liquid, and, in particular,
406 its evolution as the layer becomes heavily-enriched; such behavior is poorly
407 constrained up to date. We anticipate that D_{FeO} will actually start closer to
408 a value of 0.1 (Nomura et al., 2011) and evolve to larger values as the BMO
409 layer decreases in size, thus we believe our end-member choices for D_{FeO}
410 bracket the expected behavior. Such evolution would in turn result in highly
411 energetic dynamo for the first few hundred million years, similar to Figure
412 4E, with sustained Ohmic dissipation values beyond 2 Gyrs, resembling the
413 scenario shown in Figure 4F with the higher D_{FeO} value.

414 Our models successfully show that a crystallizing BMO can be an effec-
415 tive mechanism for generating and sustaining a dynamo throughout early

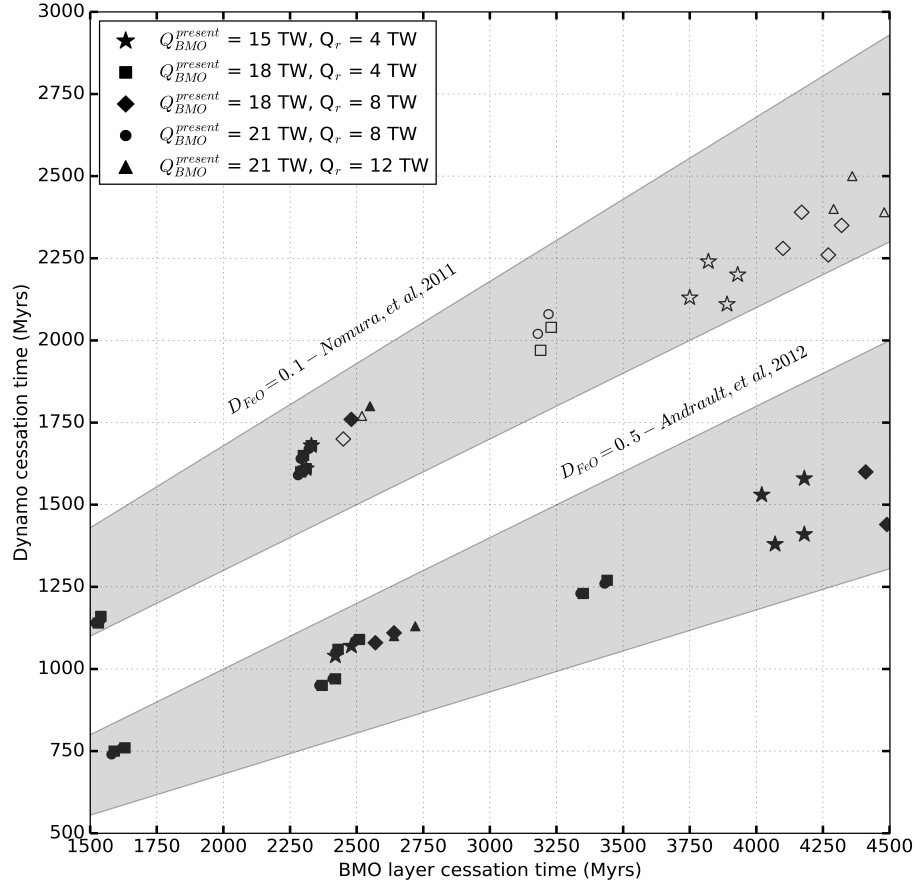


Figure 6: Duration of dynamo activity versus BMO layer crystallization time for all models that fully crystallized. Models with $E_\Phi > 0$ at $c_{FeO}^l = 50$ wt% are plotted in black (filled), while those whose E_Φ value was negative at $c_{FeO}^l = 50$ wt% are plotted in black (unfilled) at the last time E_Φ was above zero. Shaded regions as per Figure 5.

416 Earth. Most importantly, all models whose BMO layer successfully crystal-
417 lized during the age of the Earth have sufficient entropy to generate magnetic
418 activity for at least the first 1.5 Gyrs (Figure 5), with some lasting well passed
419 2 Gyrs. A vast range of parameter combinations other than the choices we
420 made would also lead to scenarios with enough entropy to generate a dynamo
421 for at least 1.5 Gyrs, conservatively. This makes a BMO-driven dynamo a
422 plausible mechanism for explaining the existence of a magnetic field early
423 on in Earth’s history as required by paleomagnetic observations; thus relax-
424 ing the need for a global magnetic field to be entirely powered by thermal
425 cooling of the core. Additionally, since exsolution-based mechanisms are also
426 contingent upon the presence of a BMO of some depth, the BMO-powered
427 dynamo is not mutually exclusive with them and the possibility exists for
428 both to operate, either contemporaneously or sequentially.

429 The time required to fully crystallize a BMO layer as well as the dura-
430 tion of a dynamo that such evolution would produce varies greatly among
431 models (Figure 6). However, it is possible to have some scenarios where a
432 dynamo can be sustained (e.g. $E_{\Phi} > 0$) for a longer time window given the
433 conservative cutoff employed here, all while also constraining its BMO layer
434 to be fully crystallized at present day and a CMB temperature in agree-
435 ment with current best estimates. Previous work emphasized that ”thermal
436 catastrophe” outcomes were constraints for model evolutions and used this
437 as a basis for determining which combinations of parameters were deemed
438 successful (Korenaga, 2013, 2008; Driscoll and Bercovici, 2014), however, by
439 these standards all of our models would be unsuccessful which demonstrates
440 this logic is not sound. Instead, we propose the only constraint that must

441 be satisfied is that the mantle with an initial BMO must completely solidify
442 within the age of the Earth, and if not, this is what we would refer to as un-
443 successful model. There is nothing catastrophic or implausible about thermal
444 evolutions that exceed the solidus temperatures for part of their evolution.

445 5. Conclusion

446 The evolution of a crystallizing basal magma ocean overlying the liquid
447 core can explain the magnetic evolution of early Earth as most models tested
448 here are energetic enough to sustain a dynamo during this time. Indeed, some
449 of the models sustain dynamos well into the Archaen, though marginally.

450 The evolution of a basal magma ocean, as modeled here, depends heavily
451 on the material properties of silicates in general and silicate melts in par-
452 ticular. Parameters such as the partitioning coefficient for a molten silicate
453 layer and its evolution as the layer becomes highly enriched in FeO (i.e.
454 $c_{FeO}^l > 50$ wt%), as well as the associated melting-point depression of such
455 a composition at near-CMB pressure and temperature conditions are crucial
456 parameters yet they are poorly constrained to date. The work presented
457 here, while it provides a novel mechanism to generate a dynamo and under-
458 stand Earth's complex magnetic history, should serve as motivation to better
459 constrain these parameters experimentally.

460 Moreover, the versatility of this model does not hinge on a specific con-
461 dition of core cooling; in fact, it can be adapted to complement thermal evo-
462 lution models involving any thermal conductivity values for the core. More
463 importantly, this model complements previous dynamo mechanism proposed
464 by being able to generate enough power to induce and sustain an early dy-

465 namo whose lifespan can be extended by different mechanism (e.g. the Mg
466 exsolution of (O'Rourke et al., 2017)). A similar computational formula-
467 tion can be relevant to simulate thermal history schemes in "super-Earth"
468 exoplanets.

469 **Acknowledgements**

470 We acknowledge C. Davies for providing the idea of calculating the en-
471 tropy budget for the BMO and for providing the code used for (Davies, 2015)
472 for us to adapt. We thank J. Badro, C. Boukare, L. Stixrude, S. Stewart for
473 helpful discussions. We acknowledge support from NSF.

474 **References**

475 Andrault, D., Petitgirard, S., Nigro, G. L., Devidal, J.-L., Veronesi, G.,
476 Garbarino, G., Mezouar, M., 2012. Solid-liquid iron partitioning in Earths
477 deep mantle. *Nature* 487 (7407), 354.

478 Anzellini, S., Dewaele, A., Mezouar, M., Loubeyre, P., Morard, G., 2013.
479 Melting of iron at Earths inner core boundary based on fast X-ray diffrac-
480 tion. *Science* 340 (6131), 464-466.

481 Badro, J., Aubert, J., Hirose, K., Nomura, R., Blanchard, I., Borensztajn,
482 S., Siebert, J., 2018. Magnesium Partitioning Between Earth's Mantle and
483 Core and its Potential to Drive an Early Exsolution Geodynamo. *Geophys-
484 ical Research Letters* 45 (24), 13-240.

485 Badro, J., Siebert, J., Nimmo, F., 2016. An early geodynamo driven by

- 486 exsolution of mantle components from Earth's core. *Nature* 536 (7616),
487 326.
- 488 Boukaré, C.-E., Ricard, Y., 2017. Modeling phase separation and phase
489 change for magma ocean solidification dynamics. *Geochemistry, Geo-*
490 *physics, Geosystems* 18 (9), 3385–3404.
- 491 Boukaré, C.-E., Ricard, Y., Fiquet, G., 2015. Thermodynamics of the MgO-
492 FeO-SiO₂ system up to 140 GPa: Application to the crystallization of
493 Earth's magma ocean. *Journal of Geophysical Research: Solid Earth*
494 120 (9), 6085–6101.
- 495 Buffett, B. A., Huppert, H. E., Lister, J. R., Woods, A. W., 1996. On the
496 thermal evolution of the Earth's core. *Journal of Geophysical Research:*
497 *Solid Earth* 101 (B4), 7989–8006.
- 498 Canup, R. M., Asphaug, E., 2001. Origin of the Moon in a giant impact near
499 the end of the Earth's formation. *Nature* 412 (6848), 708.
- 500 Caracas, R., Hirose, K., Nomura, R., Ballmer, M. D., 2019. Melt–crystal
501 density crossover in a deep magma ocean. *Earth and Planetary Science*
502 *Letters* 516, 202–211.
- 503 Čuk, M., Stewart, S. T., 2012. Making the Moon from a fast-spinning Earth:
504 a giant impact followed by resonant despinning. *Science* 338 (6110), 1047–
505 1052.
- 506 Davies, C. J., 2015. Cooling history of Earth's core with high thermal con-
507 ductivity. *Physics of the Earth and Planetary Interiors* 247, 65–79.

508 de Koker, N., Steinle-Neumann, G., Vlček, V., 2012. Electrical resistivity and
509 thermal conductivity of liquid Fe alloys at high P and T, and heat flux in
510 Earths core. *Proceedings of the National Academy of Sciences* 109 (11),
511 4070–4073.

512 De Koker, N., Stixrude, L., 2009. Self-consistent thermodynamic description
513 of silicate liquids, with application to shock melting of MgO periclase and
514 MgSiO₃ perovskite. *Geophysical Journal International* 178 (1), 162–179.

515 Driscoll, P., Bercovici, D., 2014. On the thermal and magnetic histories of
516 Earth and Venus: Influences of melting, radioactivity, and conductivity.
517 *Physics of the Earth and Planetary Interiors* 236, 36–51.

518 Du, Z., Boujibar, A., Driscoll, P., Fei, Y., 2019. Experimental constrains on
519 an MgO exsolution-driven geodynamo. *Geophysical Research Letters*.

520 Du, Z., Jackson, C., Bennett, N., Driscoll, P., Deng, J., Lee, K. K., Green-
521 berg, E., Prakapenka, V. B., Fei, Y., 2017. Insufficient energy from
522 MgO exsolution to power early geodynamo. *Geophysical Research Letters*
523 44 (22), 11–376.

524 Dziewonski, A. M., Anderson, D. L., 1981. Preliminary reference Earth
525 model. *Physics of the earth and planetary interiors* 25 (4), 297–356.

526 Fiquet, G., Auzende, A., Siebert, J., Corgne, A., Bureau, H., Ozawa, H.,
527 Garbarino, G., 2010. Melting of peridotite to 140 gigapascals. *Science*
528 329 (5998), 1516–1518.

529 Gomi, H., Ohta, K., Hirose, K., Labrosse, S., Caracas, R., Verstraete, M. J.,
530 Hernlund, J. W., 2013. The high conductivity of iron and thermal evolution

531 of the Earths core. *Physics of the Earth and Planetary Interiors* 224, 88–
532 103.

533 Gubbins, D., Alfe, D., Masters, G., Price, G. D., Gillan, M., 2003. Can
534 the Earths dynamo run on heat alone? *Geophysical Journal International*
535 155 (2), 609–622.

536 Gubbins, D., Alfe, D., Masters, G., Price, G. D., Gillan, M., 2004. Gross
537 thermodynamics of two-component core convection. *Geophysical Journal*
538 *International* 157 (3), 1407–1414.

539 Hirose, K., Morard, G., Sinmyo, R., Umemoto, K., Hernlund, J., Helffrich,
540 G., Labrosse, S., 2017. Crystallization of silicon dioxide and compositional
541 evolution of the Earths core. *Nature* 543 (7643), 99.

542 Holmström, E., Stixrude, L., Scipioni, R., Foster, A., 2018. Electronic con-
543 ductivity of solid and liquid (Mg, Fe) O computed from first principles.
544 *Earth and Planetary Science Letters* 490, 11–19.

545 Korenaga, J., 2008. Urey ratio and the structure and evolution of Earth’s
546 mantle. *Reviews of Geophysics* 46 (2).

547 Korenaga, J., 2013. Initiation and evolution of plate tectonics on Earth:
548 theories and observations. *Annual review of earth and planetary sciences*
549 41, 117–151.

550 Labrosse, S., 2003. Thermal and magnetic evolution of the Earths core.
551 *Physics of the Earth and Planetary Interiors* 140 (1-3), 127–143.

- 552 Labrosse, S., 2015. Thermal evolution of the core with a high thermal con-
553 ductivity. *Physics of the Earth and Planetary Interiors* 247, 36–55.
- 554 Labrosse, S., Hernlund, J., Coltice, N., 2007. A crystallizing dense magma
555 ocean at the base of the Earths mantle. *Nature* 450 (7171), 866.
- 556 Laneuville, M., Hernlund, J., Labrosse, S., Guttenberg, N., 2018. Crystal-
557 lization of a compositionally stratified basal magma ocean. *Physics of the*
558 *Earth and Planetary Interiors* 276, 86–92.
- 559 Lock, S. J., Stewart, S. T., Petaev, M. I., Leinhardt, Z., Mace, M. T., Ja-
560 cobsen, S. B., Cuk, M., 2018. The origin of the Moon within a terrestrial
561 synestia. *Journal of Geophysical Research: Planets* 123 (4), 910–951.
- 562 McDonough, W. F., Sun, S.-S., 1995. The composition of the Earth. *Chemical*
563 *Geology* 120 (3-4), 223–253.
- 564 McWilliams, R. S., Spaulding, D. K., Eggert, J. H., Celliers, P. M., Hicks,
565 D. G., Smith, R. F., Collins, G. W., Jeanloz, R., 2012. Phase transforma-
566 tions and metallization of magnesium oxide at high pressure and temper-
567 ature. *Science* 338 (6112), 1330–1333.
- 568 Nimmo, F., 2015. Energetics of the core: Ed. G. Schubert. *Treatise on geo-*
569 *physics* (second edition). Elsevier, Oxford 8, 27–55.
- 570 Nomura, R., Ozawa, H., Tateno, S., Hirose, K., Hernlund, J., Muto, S., Ishii,
571 H., Hiraoka, N., 2011. Spin crossover and iron-rich silicate melt in the
572 Earths deep mantle. *Nature* 473 (7346), 199.
- 573 Olson, P., 2013. The new core paradox. *Science* 342 (6157), 431–432.

- 574 O'Rourke, J. G., Korenaga, J., Stevenson, D. J., 2017. Thermal evolution
575 of Earth with magnesium precipitation in the core. *Earth and Planetary*
576 *Science Letters* 458, 263–272.
- 577 O'Rourke, J. G., Stevenson, D. J., 2016. Powering Earths dynamo with mag-
578 nesium precipitation from the core. *Nature* 529 (7586), 387.
- 579 Pozzo, M., Davies, C., Gubbins, D., Alfe, D., 2012. Thermal and electrical
580 conductivity of iron at Earths core conditions. *Nature* 485 (7398), 355.
- 581 Scipioni, R., Stixrude, L., Desjarlais, M. P., 2017. Electrical conductivity of
582 SiO₂ at extreme conditions and planetary dynamos. *Proceedings of the*
583 *National Academy of Sciences* 114 (34), 9009–9013.
- 584 Soubiran, F., Militzer, B., 2018. Electrical conductivity and magnetic dy-
585 namos in magma oceans of Super-Earths. *Nature communications* 9 (1),
586 3883.
- 587 Spaulding, D., McWilliams, R., Jeanloz, R., Eggert, J., Celliers, P., Hicks,
588 D., Collins, G., Smith, R., 2012. Evidence for a phase transition in silicate
589 melt at extreme pressure and temperature conditions. *Physical Review*
590 *Letters* 108 (6), 065701.
- 591 Stackhouse, S., Stixrude, L., Karki, B. B., 2010. Thermal conductivity of per-
592 iclase (MgO) from first principles. *Physical review letters* 104 (20), 208501.
- 593 Stevenson, D. J., 2003. Planetary magnetic fields. *Earth and planetary sci-*
594 *ence letters* 208 (1-2), 1–11.

- 595 Stixrude, L., 2014. Melting in super-earths. *Philosophical Transactions of*
596 *the Royal Society A: Mathematical, Physical and Engineering Sciences*
597 372 (2014), 20130076.
- 598 Stixrude, L., de Koker, N., Sun, N., Mookherjee, M., Karki, B. B., 2009.
599 Thermodynamics of silicate liquids in the deep Earth. *Earth and Planetary*
600 *Science Letters* 278 (3-4), 226–232.
- 601 Tarduno, J. A., Cottrell, R. D., Davis, W. J., Nimmo, F., Bono, R. K., 2015.
602 A Hadean to Paleoarchean geodynamo recorded by single zircon crystals.
603 *Science* 349 (6247), 521–524.
- 604 Tarduno, J. A., Cottrell, R. D., Watkeys, M. K., Hofmann, A., Doubrovine,
605 P. V., Mamajek, E. E., Liu, D., Sibeck, D. G., Neukirch, L. P., Usui, Y.,
606 2010. Geodynamo, solar wind, and magnetopause 3.4 to 3.45 billion years
607 ago. *Science* 327 (5970), 1238–1240.
- 608 Wolf, A. S., Bower, D. J., 2018. An equation of state for high pressure-
609 temperature liquids (RTpress) with application to MgSiO₃ melt. *Physics*
610 *of the Earth and Planetary Interiors* 278, 59–74.
- 611 Ziegler, L., Stegman, D., 2013. Implications of a long-lived basal magma
612 ocean in generating Earth’s ancient magnetic field. *Geochemistry, Geo-*
613 *physics, Geosystems* 14 (11), 4735–4742.